Distribution Category:
Materials (UC-25)

ANL/FE-83-25

ANL/FE--83-25

DE84 010571

ARGONNE NATIONAL LABORATORY
9700 South Cass Avenue
Argonne, Illinois 60439

APPLICATION OF NDE METHODS TO GREEN CERAMICS: INITIAL RESULTS

by

D. S. Kupperman, H. B. Karplus,* R. B. Poeppel, W. A. Ellingson, H. Berger,** C. Robbins,† and E. Fuller†

Materials Science and Technology Division

March 1984

* Components Technology Division, ANL
**Industrial Quality, Inc., Gaithersburg, MD
† National Bureau of Standards, Washington, DC

Blank Page

TABLE OF CONTENTS

LIST OF FIGURES

LIST OF FIGURES (continued)

LIST OF TABLES

APPLICATION OF NDE METHODS TO GREEN CERAMICS: INITIAL RESULTS

by

D. S. Kupperman, H. Karplus, R. B. Poeppel, W. A. Ellingson,
H. Berger*, C. Robbins**, and E. Fuller**

ABSTRACT

This paper describes a preliminary investigation to assess the effectiveness of microradiography, ultrasonic methods, nuclear magnetic resonance, and neutron radiography for the nondestructive evaluation of green (unfired) ceramics. The objective is to obtain useful information on defects, cracking, delaminations, agglomerates, inclusions, regions of high porosity, and anisotropy.

Microradiographs are sharper than ordinary radiographs, particularly if samples are thick (>1 cm) or of odd geometry. Another major advantage of microradiography is the capability to observe enlargements (20-40X) of an object in real time while manipulating the object. Very small (<50-μm) defects can be detected by microradiography if they are sufficiently different in density from the surrounding material. The application of microradiography to ceramics is reviewed, and preliminary experiments with a commercial microradiography unit are described.

Conventional ultrasonic techniques are difficult to apply to flaw detection in green ceramics because of the high attenuation, fragility, and couplant-absorbing properties of these materials. However, velocity, attenuation, and spectral data were obtained with pressure-coupled transducers and provided useful information related to density variations and the presence of agglomerates. The elastic anisotropy of the green state (an important parameter related to the fabrication process) and variations in dispersion (which may also be related to microstructural variations) were also successfully measured.

Nuclear magnetic resonance (NMR) imaging techniques and neutron radiography were considered for detection of anomalies in the distribution of porosity. With NMR, areas of high porosity may be detectable if the binder is burned out and replaced with a hydrogen-rich dopant such as water. Although this technique may not be applicable to screening out defective specimens, it may be useful for assessing the fabrication process.

With neutron radiography, imaging the binder distribution throughout the sample may not be feasible because of the low overall concentration of binder, but regions of high binder concentration (and thus high porosity) should be detectable.

*Industrial Quality Inc., Gaithersburg, MD
**National Bureau of Standards, Washington, DC

I. INTRODUCTION

The strength of ceramic materials is controlled by the stress necessary to enlarge a flaw of given size and orientation to a critical size, that is, a size sufficient to cause failure.[1,2] This critical size may be as small as 10-100 μm,[3] which is orders of magnitude smaller than for metals. Most ceramic materials exhibit a slow rate of crack growth which varies with temperature, stress, and environment. If these conditions are known and the material is adequately characterized as to the type and size of existing flaws, the probability of failure can be predicted; moreover, if it can be established that flaws are smaller than a predetermined critical size and the material properties meet appropriate specifications, adequate component life can be assured. Improved nondestructive evaluation (NDE) methods can facilitate detection of these small flaws. Furthermore, development of NDE methods for the unfired (green) state can result in considerable cost savings in fabricating structural components, as the final firing stage would be eliminated for defective components.

The research discussed below is part of an ongoing effort to study and develop acoustic, radiographic, and other techniques to characterize structural ceramics with regard to porosity, cracks, inclusions, and amounts of secondary phases. Since little information was found in the open literature concerning NDE for green ceramics, the approach followed in this effort included broad scoping studies to establish potentially useful NDE techniques and the major parameters that will affect the detection of defects in green ceramics.

II. SPECIMENS

Green ceramic specimens were provided by the Ceramics Group of the Materials Science and Technology Division at Argonne National Laboratory (ANL) and the Materials Chemistry Division of the National Bureau of Standards (NBS). The specimens were generally 50-60% of theoretical density and very fragile. The main experimental effort was carried out with silicon nitride disks 3.3 cm in diameter and 0.6 cm thick, silicon carbide disks of various sizes, and magnesium caluminate (spinel) disks 3.7 cm in diameter and 0.6 cm thick. Some other materials were also included. The specimens were cold-pressed with various loading pressures and additions of polyvinyl alcohol (PVA) or Carbowax (CW) binder; agglomerates were added to some of the powders. Table I provides additional information about the specimens.

III. MICRORADIOGRAPHY

Radiography[4-10] is a well-recognized and widely used NDE method. Several types of radiation can be used for radiography; these include x-rays, gamma rays, neutrons,[11,12] and charged particles.[13,14] Industrial radiographic inspection largely involves x-rays, and this report is primarily concerned with x-radiography. However, many of the following comments apply to radiography in general.

TABLE I. Green Ceramic Specimens Used in the Present Investigation

No.	Diam x Thickness (cm)	Powder Grain Size (μm)	Cold Pressing Load (MPa)	Sp. Gravity
	Si_3N_4 + <2 wt.% PVA (ANL)			
601[a]	3.3 x 0.6	<5	110	1.61
602[a]			110	1.61
603[a]			210	1.73
604[a]			210	1.75
605[a]			165	1.69
606[b]			110	1.39
607[b]			110	1.41
608[b]			165	1.45
609[b]			165	1.47
610[b]			220	1.57
611[b]			220	1.58
612[c]			137	1.66
613[c]			210	1.71
614[c]			210	1.73
615[c]			210	1.78
616[c]			210	1.80
	SiC + 10 wt.% CW[d] (ANL)			
SILC	3.3 x 1.9	<1	138	ND[e]
SI2	3.3 x 0.6		69	
SC-3	3.3 x 0.3		104	
SC-4	3.3 x 0.3		69	
SC-5	3.3 x 0.3		69	
	$YCrO_3$ + <1 wt.% PVA (NBS)			
YC-1	irregular	ND[d]	104	ND

No.	Diam x Thickness (cm)	Powder Grain Size (μm)	Cold Pressing Load (MPa)	Sp. Gravity
	$MgAl_2O_4$ (Spinel) + <1 wt.% PVA (NBS)			
NB1[f]	3.7 x 0.6	<5	210	ND
NB2[f]				1.84
NB3[f]				ND
NB4[f]				
NB5[g]				
NB6[g]				
NB7[g]				1.82
NB8[g]				ND
NB9[g]				
NB10[h]				
NB11[h]				
NB12[h]				
NB13[h]				1.85
NB14[h]				ND
	MgO + 20 wt.% CW (ANL)			
A10K	3.3 x 0.8	0.3	ND	ND
B10K			ND	ND
C20K			ND	ND
1			69	1.52
2			69	1.48
4			138	1.63
5			138	1.66
6			138	ND

[a] 2% agglomerates (10-30 μm) and deflocculant added.

[b] No agglomerates or deflocculant.

[c] With deflocculant only.

[d] Except SC-5, which contained 10 wt.% PVA.

[e] ND = not determined.

[f] No agglomerates.

[g] 2% agglomerates (75-100 μm) added.

[h] 20% agglomerates (75-100 μm) added.

With conventional radiographic methods, the difference in attenuation produced by a change of the order of 1-2% in object thickness can be visualized. Thickness or density changes of as little as 0.5% and high-contrast features as small as several micrometers in size can be detected under optimum circumstances (good geometry, thin object, low x-ray energy, fine-grain photographic film, etc.). As the contrast decreases to a few percent, the resolution capability is degraded.

Conventional x-ray images are not as sharp as one might desire because the radiation does not originate at a true point source. The minimum diameter of the source, or focal spot, is dictated by the need to dissipate the heat generated in an x-ray tube target by the electron beam. The size of the radiation source and the geometry of the image system together produce a defocusing effect referred to as geometric unsharpness, U_G (see Fig. 1).

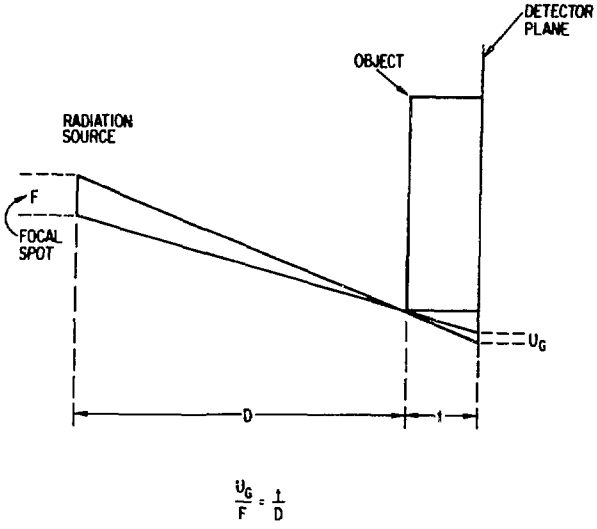

Fig. 1

Calculation of Geometric Unsharpness, U_G.

The magnitude of U_G is given by

$$U_G = \frac{Ft}{D} , \qquad (1)$$

where F = size of the radiation source, t = distance from object plane to detector, and D = distance from source to object.

The total unsharpness in a radiographic film image can be expressed as the square root of the sum of the squared values of two components[9]: (a) U_G, as defined above, and (b) unsharpness caused by vibration of the detector. For low-energy radiography, as would be used in most ceramic NDE applications, geometric unsharpness is the major factor.

A. Techniques

Microradiography[15-21] refers to the production of radiographic images that display improved spatial resolution. Generally, the term is applied to techniques that provide magnified images (usually in the range of 2 to 100X). Microradiography offers the potential capability to detect and display small inhomogeneities so they can be located, sized, and evaluated as to type and severity. This capability is important with all materials, but it is particularly important with ceramics and other brittle materials because, as discussed earlier, defects that can lead to failure tend to be relatively small (10 to 100 μm). Readily available microradiographic methods, which may be classified as either contact or projection techniques, now permit one to detect some inhomogeneities in that size range.

Contact microradiography[17,19] uses the same geometry as conventional through-transmission radiography (Fig. 1), with the object close to the detector. A fine-grained photographic film is used to produce a 1:1 radiographic image. The film can be enlarged or observed in a microscope to produce a magnified view. This works well with thin objects, for which U_g is small. With single-emulsion, slow x-ray films such as DuPont NDT 35 or Kodak R, enlargements of 10 to 20X are possible. With very slow films, as are used for lithography or spectroscopy, enlargements of 100X are possible.

Contact microradiography offers two advantages: (1) it can be accomplished with conventional x-ray equipment and (2) large areas (the size of the film) can be inspected at one time. Disadvantages of the contact method include the time required for the extra step of enlarging the image and the fact that scattered radiation from the object is readily detected; this produces an overall background in the image and thus reduces the contrast.

Projection microradiography, which is the technique of major interest for ceramic NDE applications, requires the use of a very small radiation source. For x-radiography, this typically involves a focal spot of 100 μm (0.004 in.) or less. The object is placed near the source, as illustrated in Fig. 2, to produce an x-ray image with magnification M:

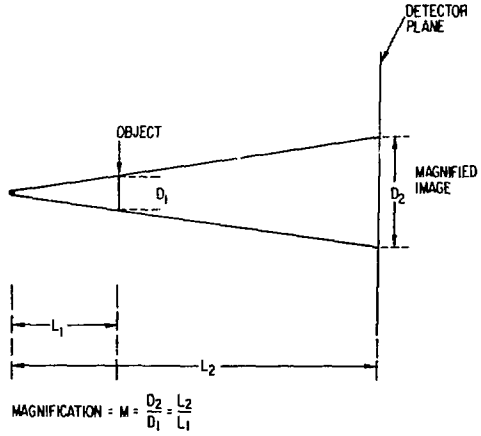

Fig. 2

Calculation of Geometric Magnification M Obtained with Projection Microradiography.

$$M = \frac{D_2}{D_1} = \frac{L_2}{L_1} \qquad (2)$$

where D_1 = object diameter, D_2 = image diameter, L_1 = source-to-object distance, and L_2 = source-to-detector distance.

In addition to improved spatial resolution, projection radiographs show improved contrast as compared to conventional radiographs because the separation between the object and the detector reduces the detection of scattered radiation.[9] Also, the enlargement of the x-ray image offers the possibility of performing radiography in real time with fast detectors, such as image intensifier systems,[22] which have inherently poorer resolution capabilities. Image intensifiers usually show a spatial resolution of 0.125 mm (4 line pairs/mm) to 0.50 mm (1 line pair/mm). For a typical 20X enlargement system, object details 10 times or more smaller than the above values should be detectable with reasonable contrast. Real-time methods offer the advantage of object manipulation to obtain the optimum radiographic view (to align a crack with the radiation beam, for example). This is important because if the alignment is off by as much as 6 degrees in a 1.25-cm (0.5 in.)-thick sample, detectability is greatly reduced.[8] A disadvantage of the projection magnification method is that only a small area of the object can be inspected at one time. For example, at 20X magnification, only about 1 cm of the object would be in a given 22.5-cm image intensifier field.

Commercially available equipment for projection microradiography is listed in Table II. The focal spot diameters given by the manufacturers vary from 5 to several hundred micrometers, although it should be noted that the exact measurement of an x-ray focal spot (commonly performed with pinhole methods)[23] is difficult. A more expensive alternative is to fabricate radioisotope sources such as ^{192}Ir in small sizes.[24]

Other approaches to the production of magnified x-ray images have been used. Good-quality single crystals can bend a monochromatic diffraction x-ray beam by asymmetric diffraction and, in effect, act as x-ray lenses.[25-27] This method, illustrated in Fig. 3, has been used with copper k-alpha radiation (about 12 keV) to produce radiographs at 100X magnification.[26] This technique is generally useful for relatively low-energy x-radiation because the crystal atomic plane spacing would tend to limit the useful x-ray wavelength.

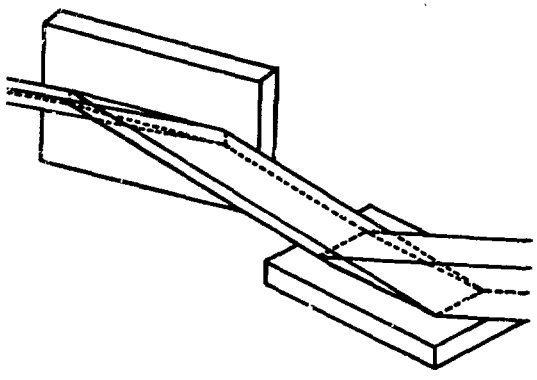

Fig. 3

Use of Asymmetric Diffraction from Two Single Crystals to Expand a Monochromatic X-Ray Beam in Two Directions. The image-carrying beam enters from the left; the expanded beam exits at the right. After Boettinger et al. (Ref. 25).

TABLE II. Availability of Microfocus X-Ray Units

Manufacturer (Country)	U.S. Supplier	Energy Range (kV)	Focal Spot Diameter (μm)	Comments
Andrex (Denmark)	a	20-150	15	Rod anode
Magnaflux (US)[b]		15-100	50	Sealed tube
Nicolet (US)[c]		20-90	10	
Pantak (England)[d]		20-160	5	
Ridge (US)[e]		10-160	10	
Rigaku (Japan)	f	30-150	200	Rod anode
Scanray (Denmark)	g	10-150	20	Rod anode
Technisch Physische Dienst (Holland)	e	150	100	Rod anode
Wardray (England)[h]		30-80	15	

[a] TFI Corp.
P.O. Box 1611
New Haven, CT 06506
Tel. (203) 934-5211

[b] Magnaflux Corp.
7300 W. Lawrence Ave.
Chicago, IL 60656
Tel. (312) 867-8000

[c] Nicolet Instrument
255 Fournier Ave.
Fremont, CA 94539
Tel. (415) 490-8300

[d] Pantak Ltd.
Vale Road
Windsor, Berks SL45UP
England
Tel. Windsor (075 35) 55611

[e] Ridge, Inc.
4432 Bibb Blvd.
Tucker, GA 30084
Tel. (404) 939-1554

[f] Rigaku, USA
3 Electronics Ave.
Danvers, MA 01923
Tel. (617) 777-2446

[g] Gamma Industries
2255 Ted Dunham Ave.
Baton Rouge, LA 70821
Tel. (504) 388-0800

[h] Wardray & Co. Ltd.
Sanford Lane
Kennington, Oxford OX15RW
England
Tel. 0865 735465

Another potentially valuable method makes use of a coded aperture or zone plate in the production of a radiograph.[28-31] The coded radiograph, produced by a coded radiation source[29] or radiation scattered from the object, is reproduced by a coherent light source (laser). The coded aperture approach has been successfully applied to imaging in nuclear medicine, where even modest improvements in spatial resolution offer advantages. Holographic reproduction of multiple x-ray images has also been reported. This approach has been considered for the creation of a three-dimensional image,[32] and also offers the potential for improved spatial resolution.[33]

Applications of microradiography are varied. It has been used for microanalysis in conjunction with the scanning electron microscope[35,36] and with synchrotron radiation.[37] Other analytical studies have involved pigment dispersion[38,39] and geological samples.[40] Observations of crystals in amorphous metals[41] and studies of crystal growth[42] have been aided by microradiography. Microstructural studies have included work with composities[43,44] to observe fiber uniformity and orientation; with concrete[45] to observe microporosity; and with metals[21,46-53] to observe alloy distribution, voids, cracks, and inclusions. The medical/biological area has also been a focal point for applications in microradiography.[18-22,28,54-56] A relatively new area of application is lithography, where needs for solid-state microcircuits have created a demand for finer electrode and circuit elements than can be fabricated by relatively long-wavelength optical methods.[20,57-60] Other inspection applications have involved welds,[48,61,62] electronic devices,[63] aerospace components[64] ceramics,[3,65-67] laser fusion targets,[25,68-71] plasmas,[31] and coated fuel particles.[34] The microradiographic methods cited here have shown capability for magnifications[50] as high as 400X and for spatial resolution[20,58] of 0.1 μm.

In ceramics, heavy inclusions such as tungsten carbide or iron usually present good x-ray contrast to the low-atomic-number host material. Detection of such high-atomic-number inclusions in the size range of 25 μm (0.001 in.) has been reported in silicon nitride and silicon carbide ceramics.[72] An example of a defect that is similar in attenuation to the host material, and thus difficult to detect even if relatively large, is a silicon inclusion in silicon nitride. Voids should be detectable if the size range fits the resolution and contrast capability of the inspection system. For example, in a 5-mm (0.2-in.)-thick specimen, a 100-μm (0.004-in.) void would represent a contrast sensitivity of 2%; this should be detectable in a ceramic sample if an x-ray energy appropriate to the material is used and U_G is less than the size of the magnified image. In a typical case, where an x-ray tube with a 10-μm focal spot is used with a source-to-object distance of 25 mm (1 in.) and a source-to-detector distance of 500 mm (20 in.), the magnification would be 20X and U_G would be 0.19 mm. The image contrast will clearly be reduced as the image size approaches and goes below the U_G value. In this example, one would predict that the projected image of a 10-μm spherical void would be slightly larger than U_G, and could therefore be detected. However, to maintain at least the 2% contrast, this size void should be in a specimen no thicker than 0.5 mm.

Volatile binders designed to be removed by firing are relatively low-atomic-number materials that should have little influence on x-ray attenuation. Therefore, radiographic differences between green and fired ceramics are expected to be relatively small.

B. Experimental Results

The limited experimental results obtained thus far for green ceramic specimens compare prints of projection microradiographs with prints of conventional radiographs that were photographically enlarged to about the same value (4X). The projection microradiographs were taken at NASA-Lewis (Cleveland, Ohio) with a microfocus unit made by the Nicolet Instrument Corporation. The unit was operated at 35 kV and had a 10-μm focal spot; the source-to-film distance was 30 cm and the source-to-object distance was 7 cm. The conventional radiographs were taken at ANL; the x-ray unit was operated at 65 kV and had a 0.5-mm focal spot. The source-to-film distance was 75 cm; the object was essentially in contact with the detector. The U_G values calculated from these geometries are 33 μm for the microfocus system and about 15 μm for the conventional radiograph; both values are sufficiently low that their influence on total unsharpness should be small.

Figure 4 shows microcracking in ceramic sample SILC (Table I), which is about 1.9 cm (0.75 in.) thick. When radiographic prints are compared, as done here, much more cracking is evident in the microfocus radiograph. The unprinted conventional radiograph showed almost all the microcracking, but with less overall clarity than the unprinted microfocus radiograph.

Figure 5 shows prints of radiographs of ceramic sample NB10 (Table I), which is 0.63 cm (0.25 in.) thick. The radiographic conditions were similar to those described above. The radiographs show small inclusions and porosity. Although the print comparison again shows a marked superiority for the microfocus radiograph, the unprinted conventional radiograph showed most of the same detail.

C. Conclusions

Analyses and literature results show that microradiography of ceramics can provide useful inspection information. The small defects that can lead to failure of ceramics can be detected by radiography under some circumstances. The experimental results obtained in this program thus far are limited. The prints comparing microfocus radiographs with enlarged conventional radiographs tend to be misleading in that the original negatives of the conventional radiographs showed much of the same detail. Nevertheless, greater clarity was noted on the microfocus radiographs.

IV. ULTRASONIC TECHNIQUES

The difficulties associated with ultrasonic examination of green ceramics are formidable. For example, low-frequency sound waves are not scattered sufficiently to allow the detection of flaws much smaller than 1 mm in size; on the other hand, sound waves with frequencies $\gtrsim$3 MHz generally undergo excessive attenuation in samples >3 mm thick. Also, ordinary couplants (e.g., water or glycerol) are often absorbed by green ceramics; this not only mitigates their coupling function, but may also affect the subsequent fabrication process. This problem can be avoided by using pressure alone to couple the transducer to the specimen, but great care is required because the applied pressure can affect the data or even result in sample breakage.

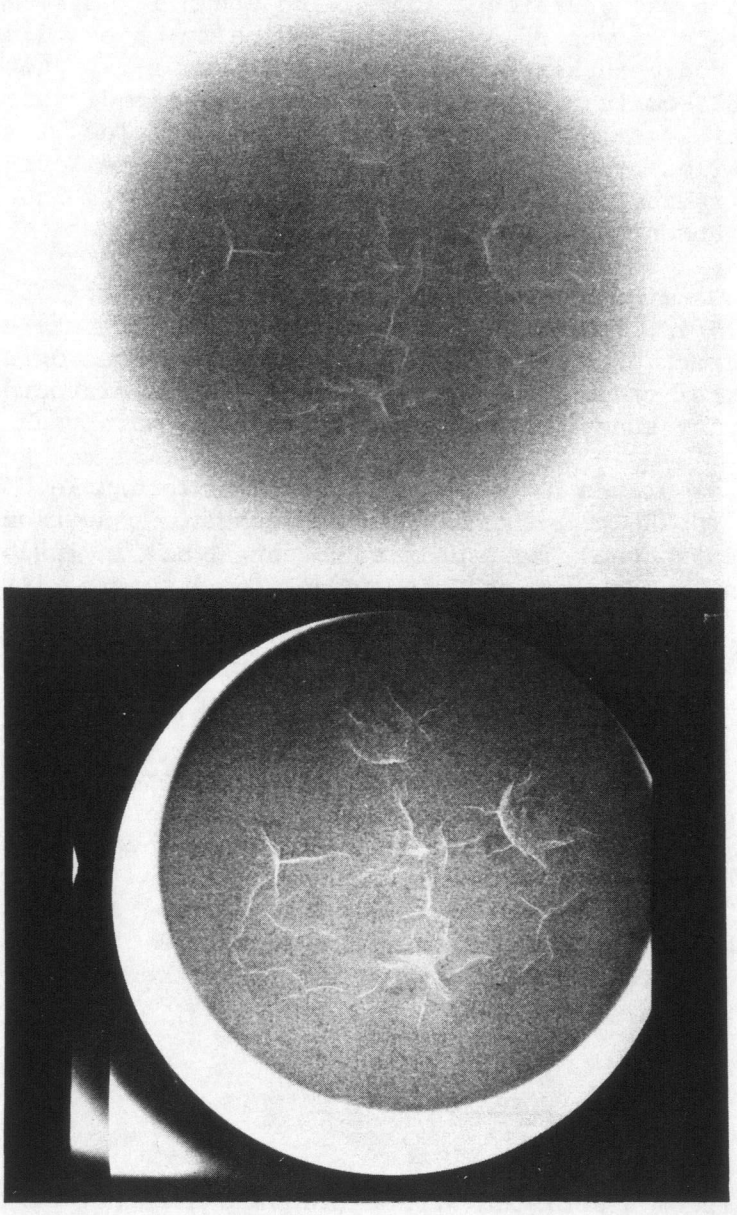

Fig. 4. Prints of a Conventional Radiograph (Top) and a Microfocus Radiograph (Bottom) of Green Ceramic Sample SILC, Showing Microcracking.

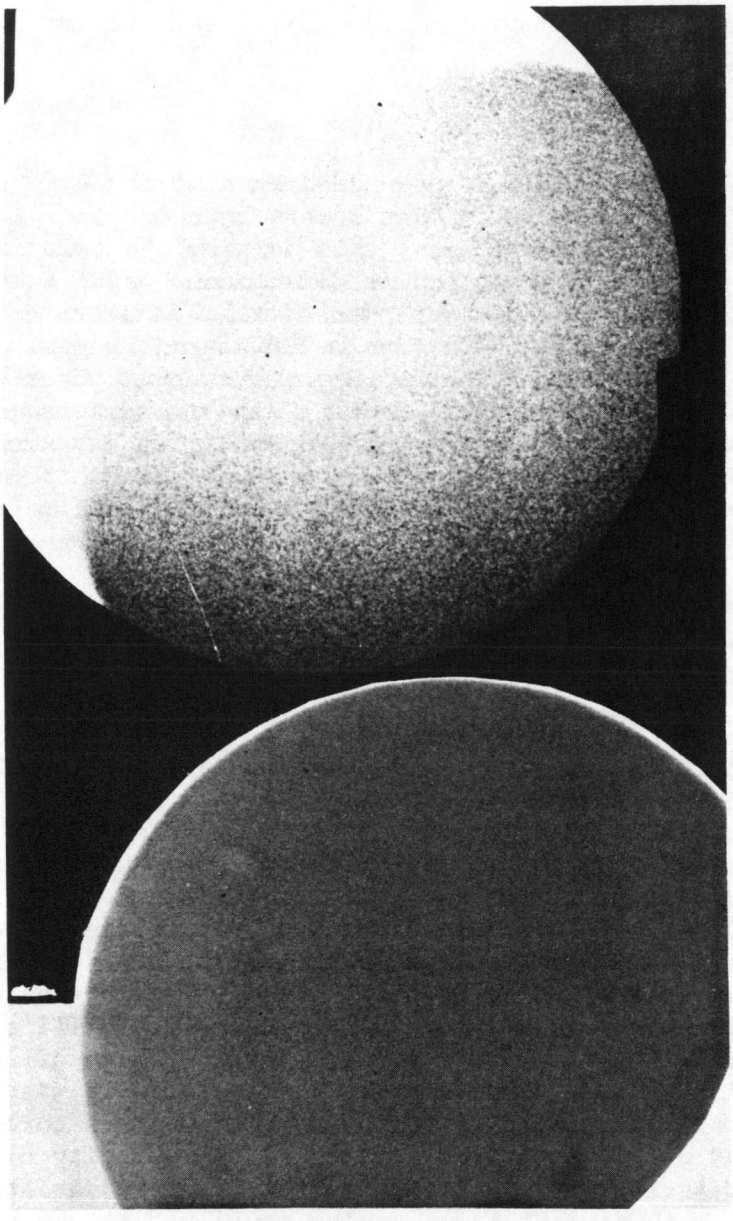

Fig. 5. Prints of a Microfocus Radiograph (Top) and a Conventional Radiograph (Bottom) of Green Ceramic Sample NB10, Showing Small Inclusions (Black Dots).

In spite of these difficulties, studies of ultrasonic attenuation and acoustic velocity (including dispersion and frequency spectra) in green ceramics may provide useful information related to density variations, porosity content, presence of agglomerates and delaminations, elastic anisotropy, and material quality in general; some examples of promising approaches are presented below. Further development of ultrasonic testing techniques, coupled with signal enhancement techniques, may lead to improved flaw detection sensitivity.

A. Elastic Anisotropy

The elastic anisotropy of a green ceramic specimen can be determined from the change in sound velocity that occurs when a shear-wave transducer is rotated with respect to the specimen, thus varying the polarization of the shear waves propagating in a particular direction. Sound velocity data were acquired for SiC, MgO, and $YCrO_3$ specimens with a Panametric 5052UAX ultrasonic transducer analyzer and a Tektronix 7904 oscilloscope with 7B85 and 7B80 time bases. Panametrix 2.25-MHz normal-incidence shear-wave transducers (13 mm in diameter) and Aerotech 2.25-MHz alpha transducers (6 mm in diameter) were employed for the measurements. The velocity was measured by overlapping successive echoes in the pulse-echo mode and determining the time delay from the oscilloscope. The time base was calibrated by checking the oscilloscope readings against a sequence of precisely timed pulses from a Tektronix type 184 time mark generator. With the SiC and MgO specimens, which have a high content of CW binder, Panametric shear-wave couplant was successfully used for both longitudinal and shear waves. With the chalk-like $YCrO_3$ specimens (<1% PVA binder), no couplant was needed for either type of wave.

Figure 6 shows the echo pattern for 2.25-MHz longitudinal and shear waves in a 3.8-mm-thick $YCrO_3$ specimen. (About 6 μs separate the first and second longitudinal echoes; about 10 μs separate the shear echoes.) Apparent attenuation is clearly rather high, on the order of 10-20 dB/cm. Furthermore, the effect of polarization on shear-wave velocity shows that the material is elastically anisotropic: A maximum velocity variation of about 3% was reproducibly observed as the shear-wave transducer was rotated about its axis while remaining over the same point on the sample. (The pressure of the transducer on the sample was controlled so that the velocity variations could not be attributed to variations in transducer loading.) Table III summarizes the sound velocity data for the $YCrO_3$ sample. The low value of Poisson's ratio implies that under stress, the volume of the specimen is significantly reduced; this is consistent with the porous, low-density nature of the sample. Since the modulus of elasticity is related to the velocity of sound, variations in shear velocity with polarization can indicate variations of modulus with direction. This variation in modulus could affect the performance of a component made from such a sample.

Table III. Sound Velocity in $YCrO_3$ Sample with PVA Binder

Longitudinal Velocity (10^5 cm/s)	Shear Velocity (10^5 cm/s)	Poisson's Ratio, σ
1.43	0.947 max	0.11
1.43	0.919 min	0.15

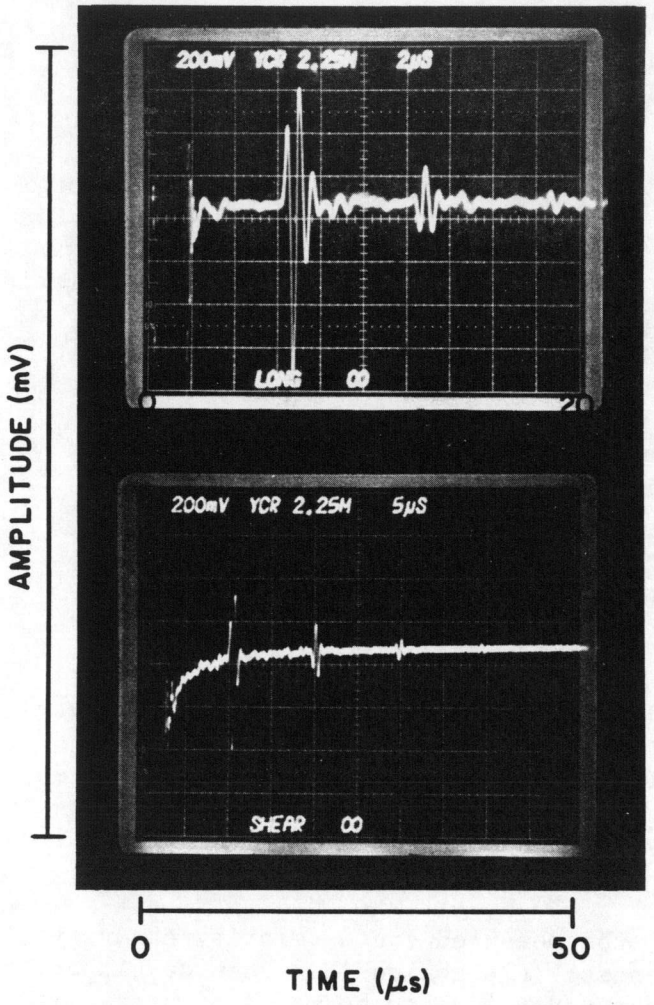

Fig. 6

Echoes from 3.8-mm-Thick $YCrO_3$ Sample Insonified with (Top) Longitudinal Waves and (Bottom) Shear Waves at 2.25 MHz. Axis dimensions are as follows: (left) 200 mV/div, (top) 2 μs/div. and (bottom) 5 μs/div.

Another example of variation with polarization was observed in a 3-mm-thick section of a spinel disk, insonified with shear waves propagating in the plane of the disk. With polarization parallel to the disk axis, the velocity (error <0.5%) was about 3.5% higher than with polarization perpendicular to the disk axis. No variation of velocity with polarization was found for wave propagation parallel to the disk axis. This implies that the shear modulus is greatest in the pressing direction.

B. Variation of Velocity with Density

The velocity of longitudinal waves has been measured as a function of density for MgO specimens with 20 wt.% CW binder. Density variations among these specimens result from differences in loading pressure, i.e., in porosity. Figure 7 shows a plot of density vs sound velocity for four samples. One of the samples is anomalous (it has a visible delamination). Based on the other three samples, a linear relationship between velocity and density is apparent; the variation in density is 1/3 the variation in velocity. Also shown in Fig. 7 is the nominal variation in density for three of the samples

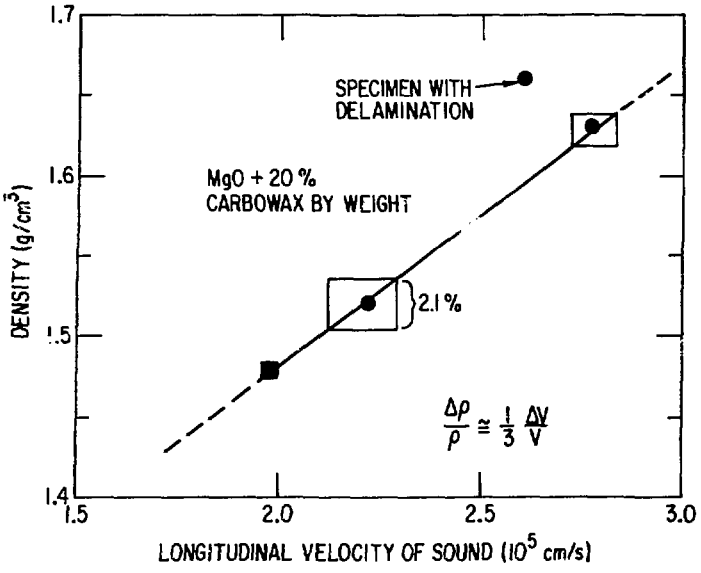

Fig. 7

Sample Density vs Longitudinal Velocity of Sound for MgO + 20% Carbowax. Rectangles show variation within each sample.

(rectangles around the data points), determined from variations in velocity measurements taken at five different points on each sample. Variations in density of up to 2% were observed. These results suggest that not only can the density (and thus porosity) of a sample be determined from sound velocity measurements, but if sufficiently small transducers were available, anomalous microstructures could be detected by mapping local variations in density.

As discussed in a later section, the measured sound velocity can vary with transducer loading in some instances. A technique has been developed that would allow through-transmission measurements to be made in water, with the transducer suspended above the sample. The sample is enclosed in a plastic "bag" which is then evacuated to assure intimate contact between sample and plastic. Tests have shown that sound can be transmitted through the immersed bag and sample, allowing velocity scans of the sample to be acquired with minimal variation in acoustic coupling. We plan to optimize this "immersion" testing technique so that sound velocity variations in green ceramic samples can be reproducibly mapped.

The maximum density (0% porosity) of MgO-20 wt.% CW, calculated from the densities of the two constituents, is 2.7 g/cm^3. The velocity obtained at this density by extrapolating the curve of Fig. 7 is 8.1 x 10^5 cm/s. This velocity can be compared to theoretical models that predict upper and lower bounds for sound velocity in a homogeneous composite material with a soft matrix and hard filler, as a function of the volume fraction of one of the constituents. Theoretical values for the longitudinal velocity were calculated as a function of volume fraction using both the Voigt model[73,74] (which assumes constant strain and gives an upper bound for velocity) and the Reuss model[73,74] (which assumes constant stress and gives a lower bound). The velocities were calculated from the modulus according to the following relationships:

$$\rho v_{\ell_V}^2 = f_1\rho_1 v_{\ell_1}^2 + f_2\rho_2 v_{\ell_2}^2 \quad \text{(Voigt velocity)}, \tag{3}$$

$$\frac{1}{\rho v_{\ell_R}^2} = \frac{f_1}{\rho_1 v_{\ell_1}^2} + \frac{f_2}{\rho_2 v_{\ell_2}^2} \quad \text{(Reuss velocity)}, \tag{4}$$

where f_1, f_2 are fractional volumes, ρ_1, ρ_2 are densities, and v_{ℓ_1}, v_{ℓ_2} are longitudinal velocities for constituents 1 and 2, respectively, and $\rho = f_1\rho_1 + f_2\rho_2$. Figure 8 shows the resultant upper (Voigt) and lower (Reuss) velocity limits for MgO/CW composites vs the volume fraction of CW. The extrapolated velocity for a volume fraction of 37.5% CW (the amount used in the ANL pellets) is indicated. This value is within the theoretical bounds and is close to the Voigt limit.

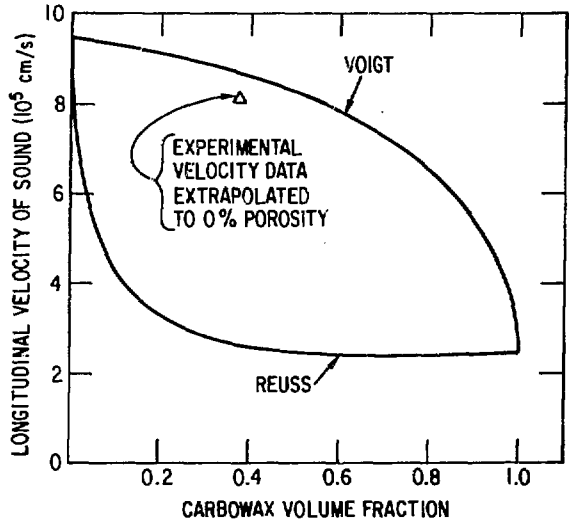

Fig. 8. Theoretical Upper and Lower Bounds for Longitudinal Velocity vs Carbowax Volume Fraction. Experimental value determined from extrapolation of data in Fig. 7 is also shown.

These results indicate that sound velocity measurements can provide quantitative information on porosity and local fluctuation in density, and can perhaps indicate anomalous microstructures. The analysis also indicates that data acquired in this manner may be predicted by models for composites, further suggesting that sound velocity data and relationships to anomalous microstructures may be understood from a fundamental point of view.

C. Effect of Agglomerates on Ultrasonic Properties

The presence of agglomerates in the green state can have deleterious effects on the properties of the ceramic specimen after firing.[75] The use of ultrasonic techniques to obtain information on the presence of agglomerates was investigated, on the assumption that ultrasonic scattering from groups of agglomerates might alter the spectral characteristics or attenuation of ultrasonic waves even if individual agglomerates could not be detected. Since ordinary attenuation is difficult to measure accurately, spectral data were examined. The wavelength of longitudinal waves is about 1.3 mm at 1 MHz. Agglomerates in the 100-μm (0.1-mm) size range should scatter in the Rayleigh region, where scattering is frequency dependent. Figure 9 shows frequency spectra (0-2 MHz) for longitudinal waves propagating in spinel disks with 0, 2, and 20 wt.% agglomerates (75-100 μm in size) in a matrix with particle size <5 μm. The spectrum for Plexiglass is also shown to permit correction for the transducer characteristics. Rayleigh scattering dominates the frequency dependence of the attenuation. Larger particles contribute more to the higher frequency scattering and thus the introduction of agglomerates is expected to accentuate the high-frequency attenuation. This appears to be the case in Fig. 9.

These results suggest that frequency data may provide qualitative information on the presence of agglomerates in green ceramics. Further efforts are obviously needed to establish the validity of this concept. The effect of agglomerates on the velocity of longitudinal and shear waves was also examined. No statistically significant difference was noted between samples with and without agglomerates.

D. Dispersion and Effects of Pressure on Velocity and Attenuation

The high attenuation of ultrasonic waves in green ceramics makes it difficult to obtain reliable ultrasonic data with standard single-transducer, pulse-echo techniques. To obtain more accurate measurements of the group and phase components of velocity, data were acquired with two transducers, placed on opposite sides of the disk specimens. The receiver could then be coupled to a high-gain, low-noise amplifier and a signal obtained even under highly attenuating conditions, without contamination by residual transducer ringing.

In order to keep transmitting and receiving transducers aligned while changing and repositioning specimens, one transducer was held in the chuck of a sturdy drill press. Weights were hung on the drill press handle to apply steady pressure. The force on the transducers was calibrated by placing a suitable force gauge in the position of the specimens. Friction in the press limited accuracy and repeatability; this problem was ameliorated with thorough lubrication, vigorous tapping with a mallet, and separate calibration of increasing and decreasing weight ranges.

To measure group velocity, impulses were sent from the transmitting transducer to the receiving transducer with and without the sample in place, and the arrival times were compared. To measure phase velocity, the phase of the through-transmission signal was compared with the phase of the transmission signal with the sample removed, and the frequency that gave 0° and 180° phase shifts between the transmitted and received wave was determined.

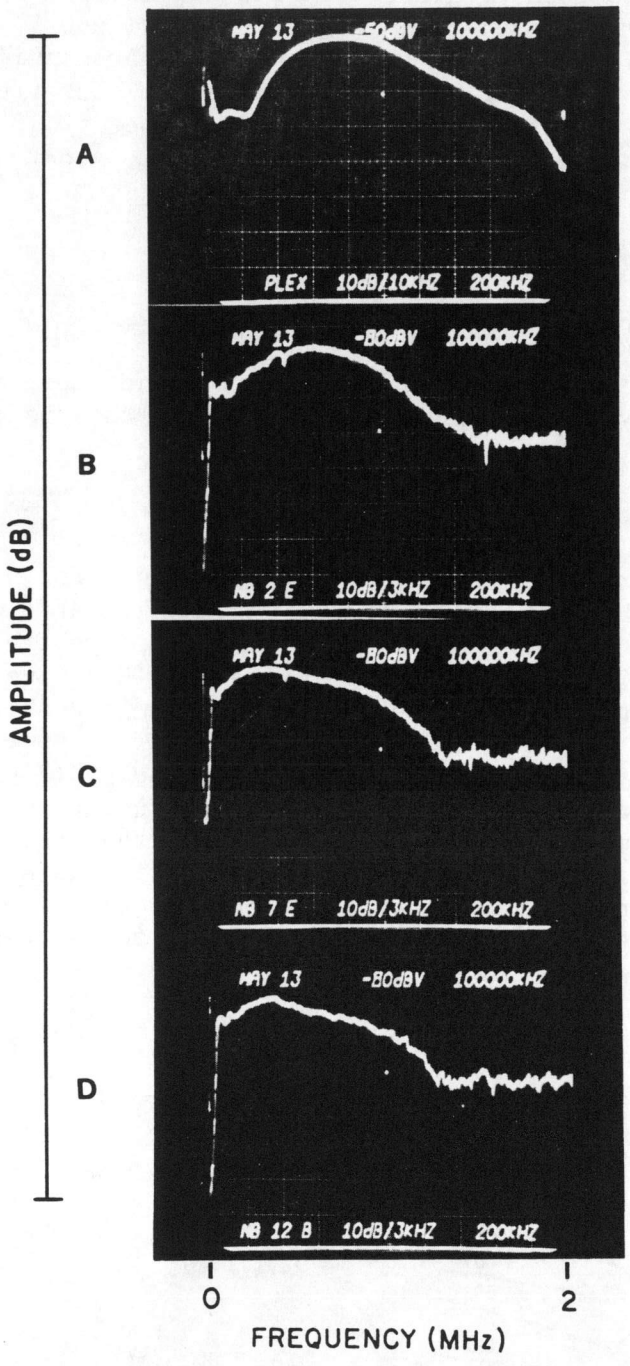

Fig. 9. Frequency Spectra for Longitudinal Waves Propagating in (A) Plexiglass and (B-D) Spinel Disks with Agglomerate Contents of (B) 0%, (C) 2%, and (D) 20%. Horizontal axis shows 200 kHz/div; vertical axis shows 10 dB/div.

The phase shift between the transmitting and receiving transducers in the absence of a sample was determined at that frequency to calculate a correction factor. The frequency was then progressively reduced until a very small number of waves (1/2, 1, or 1-1/2) could be shown unambiguously to be present in the sample. By counting the number of 0^{o} and 180^{o} phase shifts and adding ϕ, the exact number of wavelengths can be calculated at each frequency. The phase velocity c is then calculated from the whole number of 180^{o} phase shifts N, the transducer phase shift ϕ, the sample thickness L, and the frequency f, where

$$c = f\lambda \tag{5}$$

and

$$\lambda = L/(N + \phi/360). \tag{6}$$

Phase velocity is then plotted as a function of frequency and the slope dc/df is determined graphically. The group velocity, u, can then be determined from the formula

$$u = c/[1 - (f/c)(dc/df)]. \tag{7}$$

This method of determining phase velocity works only for highly attenuating samples in which the standing waves are very weak. Attenuation was estimated from the spectrum of the received pulse. The spectra were obtained by use of a Tektronix 7903 with a 3L5 plug-in module. Group velocity was found to vary with applied transducer pressure and sample density. Shear-wave velocity (Fig. 10) shows a monotonic rise with applied pressure and with increasing sample density. For longitudinal-wave velocity (Fig. 11), the rise is even steeper than for shear waves and the dependence on sample density is more complex. A few measurements with larger low-frequency transducers tend to indicate a significantly lower velocity. Caution is needed in interpreting these data in the light of the rather long-duration (low-frequency) received pulse. (Measurements were made to the first zero crossing.)

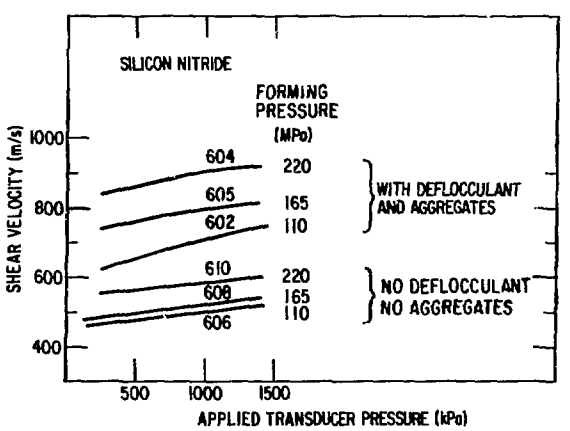

Fig. 10. Shear-Wave Velocity vs Applied Transducer Pressure for Silicon Nitride Greenware. Sample numbers (see Table I) are shown on the curves.

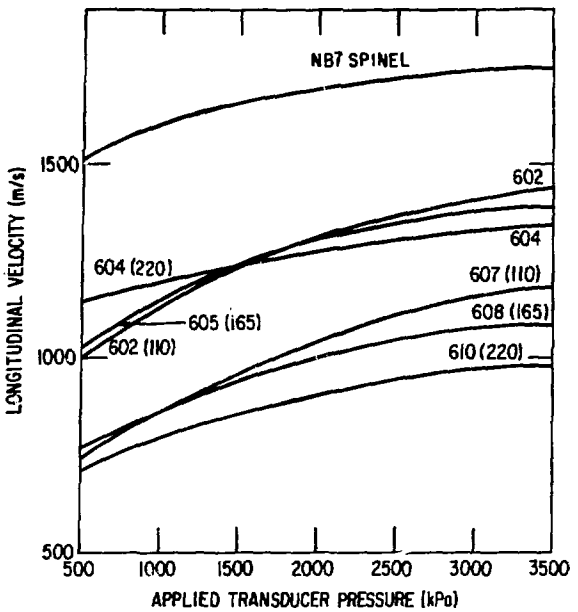

Fig. 11. Longitudinal-Wave Velocity vs Transducer Pressure for Spinel (Upper Curve) and Silicon Nitride Greenware. Sample numbers (see Table I) and forming pressures (in MPa) are shown on the silicon nitride curves.

The dispersion measurements for phase velocity (Fig. 12, dashed curves) also show a decrease in velocity at low frequencies. The order of magnitude for the calculated group velocities (Fig. 12, solid curves) agrees with the experimental values shown in Figs. 10 and 11. The spectrum obtained from a received pulse transmitted through Plexiglass is shown for reference in Fig. 13. The longitudinal waves transmitted with 2.25-MHz transducers attained higher frequencies (Fig. 14) than the shear waves (Fig. 15). Also, the spectrum and amplitude were much more strongly pressure dependent for the longitudinal waves than for the shear waves. Shear-wave transmission for the spinel samples was also very limited in frequency (Fig. 16).

E. *Conclusions*

The acoustical properties of green ceramics are obviously more complex than the properties of other familiar materials. Although the propagation of ultrasonic waves in green ceramics is subject to very high attenuation, the sensitivity of the present techniques permitted studies on samples 6-10 mm thick with longitudinal-wave frequencies as high as 3 MHz and shear-wave frequencies as high as 1.7 MHz. Strong changes in attenuation and velocity were observed with applied pressure, particularly for the higher frequency longitudinal waves. The variation of sound velocity with applied pressure may yield important information on the structure of green ceramics. Investigations of a wider range of materials, as well as the relation of the observed parameters to the properties of fired ceramics, are needed in the future.

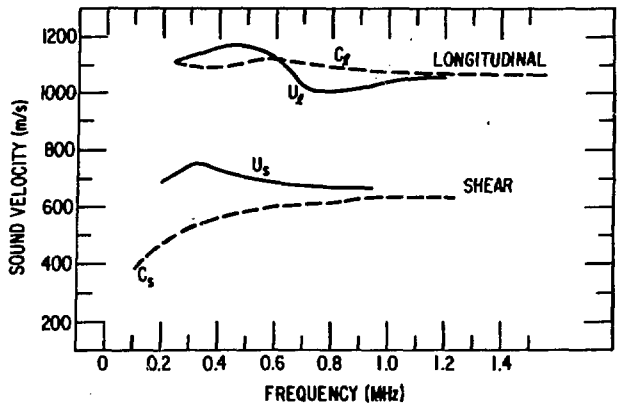

Fig. 12. Phase Velocities (Dashed Curves) and Group Velocities (Solid Curves) of Longitudinal and Shear Waves as a Function of Frequency.

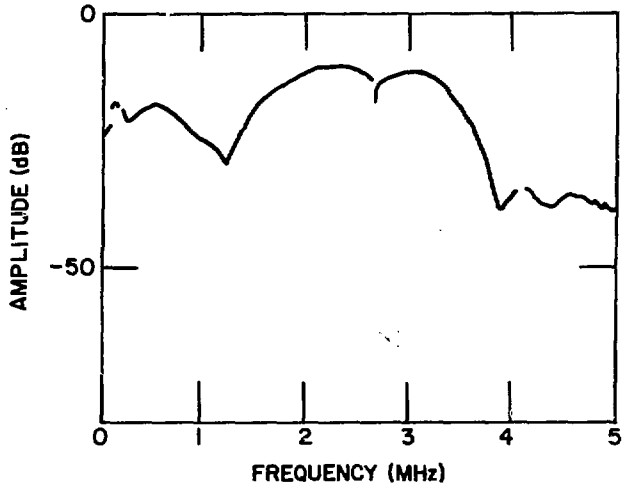

Fig. 13. Reference Transmission through Plexiglass. Horizontal axis shows 500 kHz/div; vertical axis shows 10 dB/div. (Traced from photograph.)

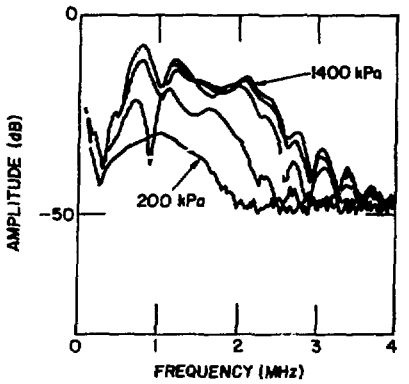

Fig. 14

Variation of Received Longitudinal-Wave Spectrum with Transducer Pressure. The attenuation decreases with increasing pressure in the range from 200 to 1400 kPa. (Traced from photograph.)

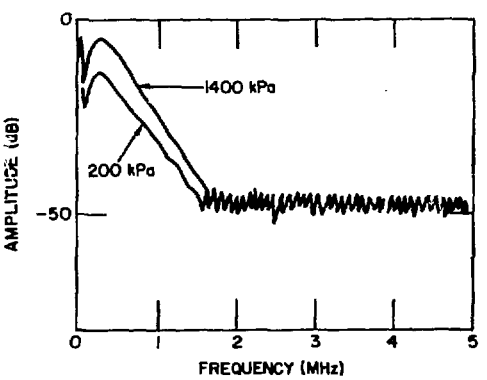

Fig. 15

Comparison of Received Shear-Wave Spectra Obtained with Transducer Pressures of 200 and 1400 kPa. (Traced from photograph.)

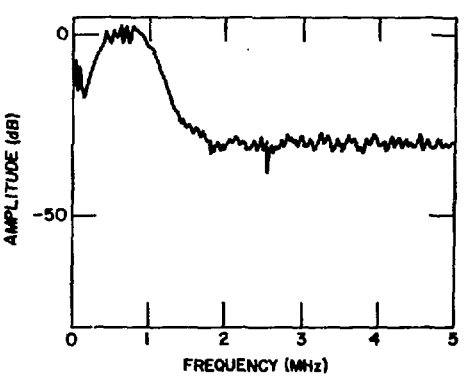

Fig. 16

Shear-Wave Spectrum for Spinel Sample NB2. (Traced from photograph.)

V. UNCONVENTIONAL TECHNIQUES

A. Nuclear Magnetic Resonance

An important objective of NDE for green ceramics is to establish the distribution of porosity and, in particular, the presence of pores on the order of 100 μm or larger. Since the pores of green ceramics are filled with a hydrogen-rich binder, they will be rich in protons. Therefore, nuclear magnetic resonance (NMR) was considered as a possible method for detecting and imaging the pores.

The technology of NMR imaging is discussed in detail in Refs. 76-78. Briefly, NMR is a quantum mechanical phenomenon observed in atomic nuclei that have spin and thus a small magnetic moment. The nuclei tend to align themselves with an externally applied magnetic field. The resonant oscillation (precession) of the nuclei during the alignment process is the NMR phenomenon. The frequency of precession (Larmor frequency) is proportional to the applied magnetic field and, in practice, occurs in the radio frequency (RF) band. To observe an NMR signal, a second time-dependent magnetic field (at the Larmor frequency) must be added to the static field. An induced signal following an RF pulse is detected by a tuned RF coil.[78] If a magnetic gradient is added, then the Larmor frequency will vary spatially across a specimen. After Fourier transformation, the NMR signal takes the form of a wave related to the shape of the sample. Computer techniques similar to those used in x-ray tomography are employed to obtain three-dimensional spatial information.

A preliminary evaluation of NMR imaging has been carried out in cooperation with the General Electric Medical Systems Division, New Berlin, WI. The objective of the initial feasibility tests was to establish whether commercially available NMR tomographic imaging technology could be applied to green ceramics. Detection of PVA binder proved to be extremely difficult, but tests with water-doped SiC were encouraging. These initial tests were conducted with equipment designed for medical rather than structural-ceramics applications, but the system could be modified to enhance the sensitivity for application to ceramic materials.

Silicon carbide disk SILC was doped with water (∿3% by weight) and then cold pressed. Figure 17 shows axial views of two volumetric slices of the disk, each 8 mm in axial length, which were visible because of their proton-rich regions (water-filled pores); their positions are indicated by circles. An orthogonal view is seen in Fig. 18. The two views are consistent with respect to the distribution of proton-rich areas. Quantitative information can also be obtained from the intensity of the image. The use of a smaller coil would enhance the sensitivity and make it possible to resolve volumes as small as 100 μm.

Since the introduction of water (possibly as steam) to fill the interconnecting porosity network may have an adverse effect on the final fired component, the most likely application of NMR techniques would be in the development of processing techniques rather than in screening components before firing.

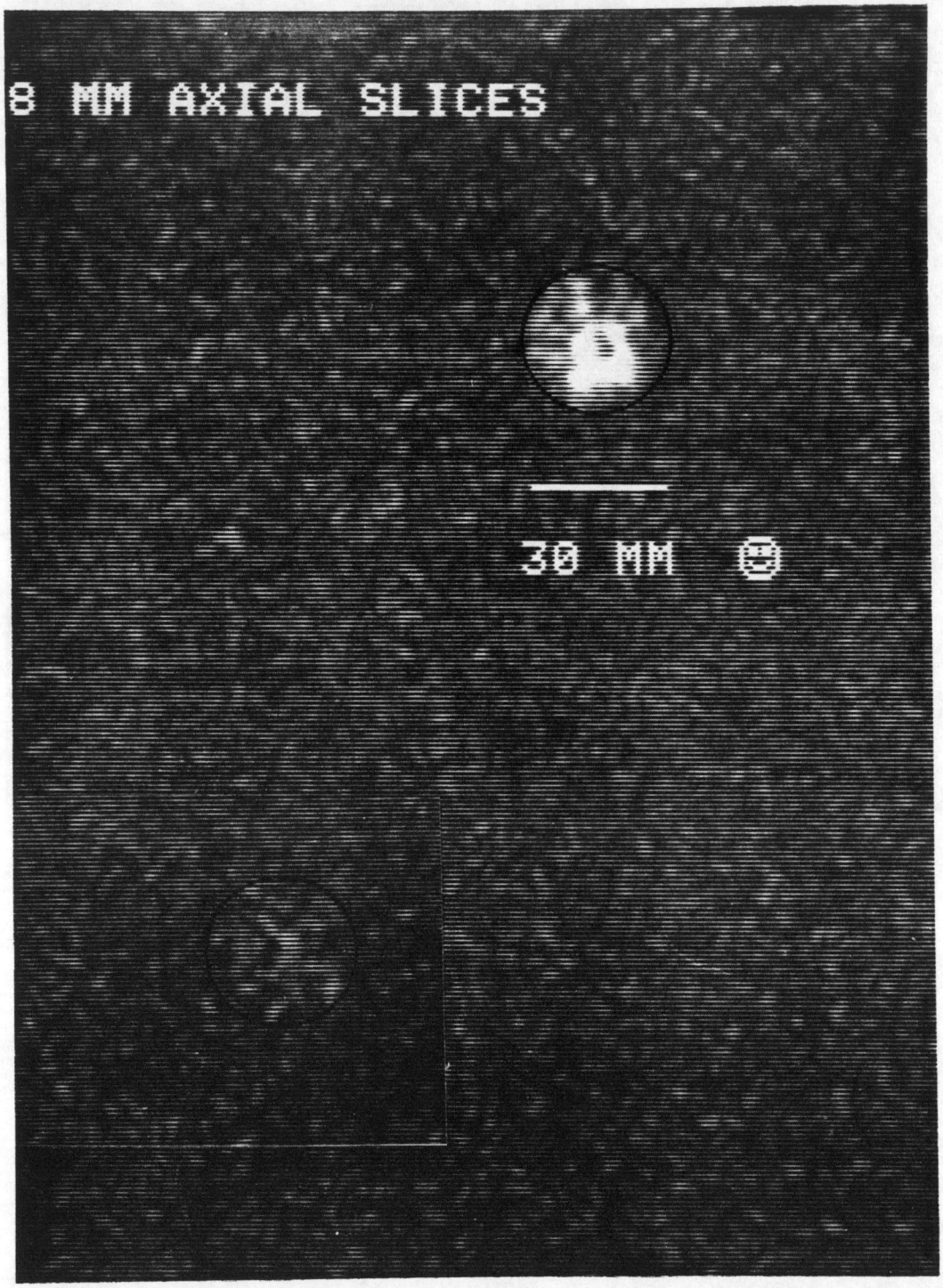

Fig. 17. NMR Image of Slices Through a Water-doped SiC Disk (Axial View). Two images of the same sample are evident. The upper right shows a center portion and the lower left a section near the sample edge. The white areas indicate the presence of water.

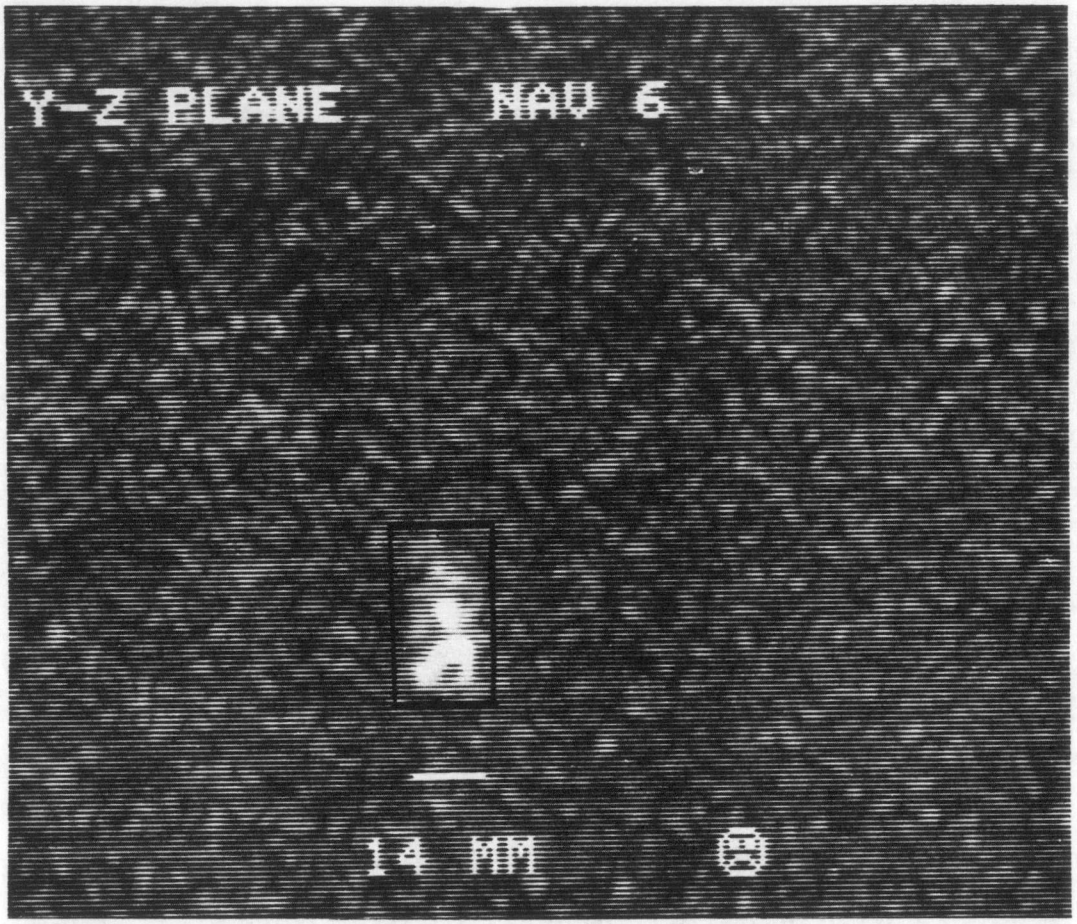

Fig. 18. NMR Image of Same Sample as Fig. 17 (Side View).

B. Neutron Radiography

Hydrogen-rich binders will also have relatively high neutron cross sections. Therefore, neutron radiography[79] was also considered for the detection of areas with a high concentration of binder.

The relative intensity of radiation that will be transmitted through an object under inspection is given by

$$I = I_o e^{-\mu x}, \tag{8}$$

where I is the radiation transmitted through an object of thickness x (in cm) and linear absorption coefficient μ (in cm^{-1}).

The absorption coefficients[80] for glass (0.22 cm^{-1}) and polyethylene (3.5 cm^{-1}) were used to estimate the likelihood of detecting the PVA binder in a 0.6-cm-thick green ceramic (spinel) sample as follows:

$$I/I_o \text{ (ceramic)} = e^{-\mu x} = 0.87;$$

$$I/I_o \text{ (ceramic + 1\% binder)} = e^{-(\mu_1 x_1 + \mu_2 x_2)} = 0.81.$$

Thus, the binder reduces transmission by ~7%. From the characteristic curve for Kodak "R" film (automatic processing) at a density of 2.0, one can calculate that a 7% change in exposure will lead to a film variation of ±0.04 density units, about twice the minimum detectable variation. Thus, it appears that a 1% concentration of binder should be observable.

Thermal neutron radiographs of sample NB1 (with PVA binder) and NB14 (from which the binder had been burned out) were prepared by Aerotest Operations, San Ramon, California. The samples were placed side by side, and successive radiographs were made with varying average film densities. Unfortunately, no difference between the samples could be detected, partly because neither sample had a uniform radiographic density. Future efforts will concentrate on preparing standards with varying amounts of PVA to establish the sensitivity of this technique, and on increasing the sensitivity by use of cold neutrons.

VI. SUMMARY

A preliminary investigation was carried out to assess the effectiveness of microradiography, ultrasonic methods, nuclear magnetic resonance, and neutron radiography for the nondestructive evaluation of green (unfired) ceramics. The objective was to obtain useful information on defects, cracking, delaminations, agglomerates, inclusions, regions of high porosity, and anisotropy.

Microradiographs are sharper than ordinary radiographs, particularly if samples are reasonably thick (>1 cm) or of odd geometry. Another major advantage of microradiography is the capability to observe enlargements (20-40X) of an object in real time while manipulating the object. Preliminary experiments were carried out with a commercial microradiography unit (courtesy of NASA-Lewis). Very small (<50-μm) defects can be detected by microradiography if they are sufficiently different in density from the surrounding material. Voids are much more difficult to detect than high-density inclusions.

Conventional ultrasonic techniques are difficult to apply to flaw detection in green ceramics because of the high attenuation, fragility, and couplant-absorbing properties of these materials. However, it proved possible to couple longitudinal- and shear-wave transducers to green specimens by pressure alone. The amount of pressure strongly affected the measured velocity and attenuation, particularly for high-frequency longitudinal waves, and this was taken into account. Velocity, attenuation, and spectral data were shown

to provide useful information on density variations and the presence of agglomerates. The elastic anisotropy of the green state (an important parameter related to the fabrication process) and variations in dispersion (which may also be related to microstructural variations) were also successfully measured. Future efforts will establish the correlation of these parameters with the ultimate performance of the fired material.

A nuclear magnetic resonance imaging technique was considered for detection of porosity in the green state. When the binder was burned out and replaced with a proton-rich dopant such as water, areas of high porosity could be detected. Neutron radiography was considered for detection of anomalies in the distribution of binders, which have a relatively high neutron cross section. Although imaging the binder distribution throughout the sample may not be feasible because of the low overall concentration of binder, regions of high binder concentration should be detectable.

ACKNOWLEDGMENTS

The authors wish to thank Aerotest Operations for providing the neutron radiographs, G. Glover and L. Edelheit of General Electric Medical Systems for providing access to NMR imaging equipment, S. Klima for providing access to the NASA microradiography facility, and R. Lanham and J. Picciolo of ANL for technical assistance on this project. The authors also wish to thank E. Stefanski for editing this manuscript.

REFERENCES

1. A. G. Evans, G. S. Kino, P. T. Khuri-Yakub, and B. R. Tittman, Failure Prediction in Structural Ceramics, Mater. Eval. 35 (4), 85-96 (1977).

2. G. S. Kino, Nondestructive Evaluation, Science 206, 173-180 (1979).

3. K. Goebbels and E. Reiter, "Non-Destructive Evaluation of Ceramic Gas Turbine Components by X-Rays and Other Methods," in Progress in Nitrogen Ceramics, F. L. Riley, ed., Martinus Nijhoff Publ., Boston and the Hauge (1983), pp. 627-634.

4. Anon., Nondestructive Examination, ASME Boiler and Pressure Vessel Code, Section V., ANSI/ASME PVB-V, ASME, New York (1983).

5. Anon., Radiography in Modern Industry, Eastman Kodak Co., Rochester, New York, Fourth Edition (1980).

6. Anon., Nondestructive Inspection and Quality Control, Metals Handbook, Vol. 11, ASM, Metals Park, Ohio (1976), pp. 105-156.

7. L. Bryant ed., Radiography and Radiation Methods, Nondestructive Testing Handbook, Vol. 3, ASNT, Columbus, Ohio (1983).

8. R. Halmshaw ed., Physics of Industrial Radiology, Heywood Books, London (1966).

9. R. Halmshaw, Industrial Radiography - Theory and Practice, Applied Science Publishers, London (1982).

10. R. C. McMaster ed., Nondestructive Testing Handbook, two volumes, Ronald Press, New York (1959).

11. H. Berger, Neutron Radiography, Elsevier, Amsterdam (1965).

12. H. Berger ed., Practical Applications of Neutron Radiography and Gaging, ASTM STP 586, ASTM, Philadelphia (1976).

13. A. M. Koehler and H. Berger, "Proton Radiography", in Research Techniques in Nondestructive Testing, Vol. 2, R. S. Sharpe, ed., Academic Press, London and New York (1973), pp. 1-30.

14. D. West and A. C. Sherwood, Proton-Scattering Radiography, Nondestr. Test. (Chicago), (October 1973), pp. 249-258.

15. V. E. Cosslett and W. C. Nixon, X-Ray Microscopy, Cambridge Monographs in Physics, Cambridge University Press, Cambridge (1960).

16. E. H. Rodgers, A Report Guide to Autoradiographic and Microradiographic Literature, Report No. MS-64-10, Army Materials and Mechanics Research Center, Watertown, Massachusetts (August 1964).

17. V. Freitag, W. Stetter and P. Charbit, The Technique of Contact Microradiography, Electromedica (W. Germany) 2, 45-49 (1974).

18. J. Braunbeck, X-Ray Microscopy, Laser Elektro-Opt. (Germany) 8, 28-30 (1976).

19. E. Spiller, R. Feder and J. Topalian, Lithography and Microscopy with X-Rays, Phys. Technol. 8, 22-28 (1977).

20. R. S. Sharpe, Projection Microradiography, J. Microsc. (Oxford) 117, Pt. 1, 123-43 (1979).

21. G. Schmahl, D. Rudolph, and B. Nieman, A New Look into the Subject: X-Ray Microscopy, Recherche 12, 1136-37 (1981); R. W. McClung, Studies in Contact Microradiography, Mater. Res. Stand. 4(2), 66-69 (February 1964); B.E. Foster, E. V. Davis, and R. W. McClung, High Resolution Boreside Radiography of Small Diameter Tube-to-Tubesheet Welds, ORNL-5474 (February 1979).

22. R. W. Parish, Fine Focus X-Ray Fluoroscopy, Br. J. Nondestr. Test. 24, 210-213 (1982).

23. Anon., X-Ray Focal Spot Size, Method of Measurement, Federal Standard No. 83, U.S. Government Printing Office, Washington, DC (May 29, 1956).

24. F. N. Case, "Preparation of Very Small Point Sources for High Resolution Radiography," in Proc. ERDA Symp. on X- and Gamma-Ray Sources and Applications, Univ. of Michigan, Ann Arbor (1976), pp. 23-24.

25. M. J. Boyle, Grazing Incidence X-Ray Microscopy of Laser Fusion Targets, Proc. Soc. Photo-Opt. Instrum. Eng. 106, 86-92 (1977).

26. W. J. Boettinger, H. E. Burdette, and M. Kuriyama, X-Ray Magnifier, Rev. Sci. Instrum. 50, 26-30 (1979).

27. R. H. Price, "X-Ray Microscopy Using Grazing Incidence Reflection Optics," in Proc. Top. Conf. on Low Energy X-Ray Diagnostics, AIP Conf. Proc. No. 75, Am. Inst. of Physics, New York (1981), pp. 189-199.

28. H. H. Barrett, Fresnel Zone Plate Imaging in Nuclear Medicine, J. Nucl. Med. 13, 382-385 (1972).

29. H. H. Barrett, K. Garewal, and D. T. Wilson, A Spatially-Coded X-Ray Source, Radiology 104, 429-430 (1972).

30. M. D. Tipton, J. E. Dowdey, and H. J. Caulfield, Coded Aperture Imaging with On-Axis Fresnel Zone Plates, Opt. Eng. 12, 166-168 (1973).

31. N. M. Ceglio, X-Ray Microscopy of Laser Fusion Plasmas Using Coded Imaging Techniques, Proc. Soc. Photo-Opt. Instrum. Eng. 106, 55-62 (1977).

32. W. A. Ellingson and H. Berger,"Three-Dimensional Radiographic Imaging," in Research Techniques in Nondestructive Testing, R. S. Sharpe, ed., Vol. 4, Academic Press, London and New York (1980), pp. 1-28.

33. V. V. Aristov and G. A. Ivanova, On the Possibility of Utilizing Holographic Schemes in X-Ray Microscopy, J. Appl. Crystallogr. 12, 19-24 (1979).

34. K. Iwamoto and K. Ikawa, Techniques for Quality Inspection of Coated Fuel Particles, J. Nucl. Sci. Technol. 12(7), 450-455 (1975).

35. D. J. Pugh and P. D. West, X-Ray Microradiography in The Scanning Electron Microscope or Microanalyzer, J. Microsc. (GB) 103, 227-38 (1975).

36. H. R. F. Horn and H. Waltinger, "X-Ray Absorption Microanalysis in the Scanning Electron Microscope," presented at the Joint Session on Electron Microscopy, Liege University (September 1973).

37. S. Lowenthal, "High Resolution X-Ray Microscopy with Synchrotron Radiation Used for Chemical Microanalysis," in Proc. 11th Cong. Int. Commission for Optics, Madrid, Spain, 1978, p. 147.

38. J. Homer and W. J. Ferguson, Examination of Titanium Dioxide Dispersion in Plastics Applying Contact Microradiography and Scanning Electron Microscope Techniques, Kunstst. Plast. (Munich) 70(1), 22-23 (November 1980).

39. C. G. Waterfield and J. Peacock, "Dispersion of Titanium Pigment in Solids," in Proc. 31st Ann. Tech. Conf. SPE, Montreal, Canada, May 1973, pp. 393-396.

40. F. Polack, S. Lowenthal, Y. Petroff, and Y. Farge, Chemical Microanalysis by X-Ray Microscopy Near Absorption Edge with Synchrotron Radiation (Geological Samples), Appl. Phys. Lett. 31(11), 785-87 (1976).

41. J. L. Walter, J. D. Livingston, and A. M. Davis, Cast-In Crystals in Amorphous Alloy Ribbons," Mater. Sci. Eng. 49(1), 47-56 (1981).

42. D. K. Bowen, "Microradiography and Absorption Microscopy," in Proc. NATO Advanced Study Institute on Characterization of Crystal Growth Defects by X-Ray Methods, Plenum Press, New York (1980), pp. 506-511.

43. F. Polato, P. Parrini, and G. Giamotti, "New Technique for the Measurement of Glass Fiber Orientation in Composite Materials," in Proc. Int. Conf. On Composite Material, Paris, 1980 (Intl. Series on the Strength and Fracture of Materials and Structures, Pergamon Press, Oxford, England (1980), pp. 1050-58.

44. P. F. Bright, R. J. Crowson, and M. J. Folkes, A Study of the Effect of Injection Speed on Fibre Orientation in Simple Mouldings of Short Glass Fibre-Filled Polypropylene, J. Mater. Sci. (GB) 13(11), 2497-2506 (1978).

45. J. Bhargava and A. Rehnstrom, Quantitative Microradiography of Concrete Using Color Film, J. Mater. 7(1), 25-27 (1972).

46. S. Pieruschothaman, N. F. Panayotou, and J. K. Tien, Synchrotron Radiation Microradiography of Cracks in Aluminum Alloys, Metall. Trans. A 11A(4), 621-25 (1980).

47. N. M. Ceglio, The Impact of Microfabrication Technology on X-Ray Optics," in Proc. Topical Conf. on Low Energy X-Ray Diagnostics, AIP Conf. Proc. No. 75, Am. Inst. of Physics, New York (1981), pp. 210-222.

48. J. F. Shackelford, Microradiography of Electron Beam Braze Joints, Lawrence Livermore Laboratory Report UCID-18813 (1980).

49. L. J. Stump and W. A. Miller, Applications of Microradiography EM-1, Prakt. Metallogr. 10(11), 636-644 (1973).

50. H. Dichtl, X-Ray Microradiography - A Metallographic Working Method, Prakt. Metallogr. 10(9), 493-501 (1973).

51. I. G. Davies, K. Haslam, and M. Randle, Contact Micro-Radiography and Its Application to Inclusion Studies, Metallography 6(4), 283-294 (1973).

52. M. McLean, The Kinetics of Spheroidization of Lead Inclusions in Aluminum, Philos. Mag. (GB) 27(6), 1253-66 (1973).

53. J. W. Christian, Progress Report on Recent Advances in Physical Metallurgy, II. Dislocation Morphology, Int. Metall. Rev. (GB) 18, 24-31 (1973).

54. J. Kirz and D. Sayre, "Soft X-Ray Microscopy of Biological Specimens," in Synchrotron Radiation Research, H. Winick and S. Doniach, eds., Plenum Press, New York (1980), pp. 277-322.

55. F. A. Young, M. Spector, and C. H. Kresch, Porous Titanium Endosseous Dental Implants in Rhesus Monkeys: Microradiography and Histological Evaluation, J. Biomed. Mater. Res., 13(6), 843-856 (1979).

56. J. Dziukowa, J. Buraczewski, and M. Dabska, Case Studies of Microradiographic Examination of Bone Tumors, Nowotwory 22, 221-226 (1973).

57. J. Bailey, Y. Ettinger, A. Fisher, and R. Feder, Evaluation of the Gas Puff X Pinch as an X-Ray Lithography and Microscopy Source, Appl. Phys. Lett. 40(1), 33-35 (1982).

58. R. A. Gutchek and J. J. Muray, Intense Plasma Source for X-Ray Microscopy, Proc. Soc. Photo-Opt. Instrum. Eng. 316, 196-202 (1981).

59. D. J. Nagel, J. M. McMahon, R. R. Whitlock, J. R. Greig, R. E. Pechacek, and M. C. Pekarar, Jpn. J. Appl. Phys. 17 (Suppl. 17-2), 472-475 (1978).

60. E. Spiller, R. Feder, and J. Topalian, X-Ray Lithography and X-Ray Microscopy, Phys. Bl. 32(12), 564-571 (1976).

61. B. E. Foster, and R. W. McClung, A Study of X-Ray and Isotopic Techniques for Boreside Radiography of Tube-to-Tubesheet Welds, Mater. Eval. 35(7), 43-48 (1977).

62. L. A. Fontijn and R. S. Peugeot, An Operational 150 kV Microfocus Rod Anode X-Ray System for NDT, NDT Int. 11(5), 229-232 (1978).

63. R. W. Parish and P. E. Kear, "High-Definition Radioagraphy of Electronic Components," in Proc. Int. Microelectronics Conf., Brighton, UK, October 1977, pp. 40-42.

64. Anon., High Definition Radiography, Aircr. Eng. 53(3), 17-18 (1981).

65. R. W. Parish and D. W. J. Cason, High Definition Radiography of Cast Turbine Blades, NDT Int. 10(4), 181-185 (1977).

66. W. N. Reynolds and R. L. Smith, The Detection of Small Defects in Ceramic Materials: A Comparison of Ultrasonic and Radiographic Methods, Br. J. Nondestr. Test. 24, 145-151 (1982).

67. H. Reiter and K. Goebbels, "Detection of Microscopic Defects by High-Frequency Ultrasonics and Microfocus X-Ray Techniques," in Proc. 10th World Conf. on Nondestructive Testing, Moscow, 1982, Paper 2-11.

68. B. W. Weinstein, Physical Measurements of Inertial Fusion Targets, J. Vac. Sci. Technol. 20(4), 1349-54 (1982).

69. R. M. Singleton and T. J. Weir, Microradiographic Characterization of Metal and Polymer Coated Microspheres, J. Vac. Sci. Technol. 18, 3 (1981).

70. G. M. Halpern, Microfabrication and Microcharacterization Techniques for Laser Fusion Targets, J. Vac. Sci. Technol. 17(5), 1184-94 (1980).

71. R. H. Day, R. P. Kruger, R. P. Whitman, and T. L. Elsberry, X-Ray Microradiography of Laser Fusion Targets, Proc. 8th Ann. Conf. Microbeam Analysis Soc. 12, 58A-E (1977).

72. B. T. Khuri-Yakub, "Nondestructive Evaluation of Structural Ceramics," in Encyclopedia of Materials Science and Engineering, H. Berger, NDE Subject Editor, Pergamon Press, Oxford, in press.

73. O. L. Anderson, "Determination of Some Uses of Isotropic Elastic Constants of Polycrystalline Aggregates Using Single Crystal Data," in Physical Acoustics, Vol. 111b, W. P. Mason, ed., Academic Press, New York (1965), pp. 43-95.

74. S. Lees and C. L. Davidson, Ultrasonic Measurement of Some Mineral Filled Plastics, IEEE Trans. Sonics Ultrason. SU-24(3), 222 (May 1977).

75. F. F. Lange, "Panel Discussion on New Directions for Fabrication Reliability," presented at Energy Materials Coordinating Contractors Meeting on Problems and Opportunities in Structural Ceramics, September 29-30, 1982, Germantown, MD.

76. I. L. Pykett, NMR Imaging in Medicine, Sci. Am., pp. 78-88 (May 1982).

77. P. Manfield and P. G. Morris, NMR Imaging in Biomedicine, Academic Press, New York (1982).

78. P. A. Battomley, Nuclear Magnetic Resonance: Beyond Physical Imaging, IEEE Spectrum, p. 32 (February 1983).

79. H. Berger, Neutron Radiography, Elsevier Publishing Co., New York (1965).

80. Anon., "Standard Practices for Thermal Neutron Radiography of Materials," in 1983 Annual Book of ASTM Standards, Section 3, ASTM, Philadelphia (1983), pp. 669-685.

Distribution for ANL/FE-83-25

Internal:

M. J. Bernard
T. D. Claar
T. N. Claytor
J. B. Darby
T. Easler
W. A. Ellingson (5)
F. Y. Fradin
B. R. T. Frost
E. L. Hartig
L. R. Johnson
H. B. Karplus (5)
K. L. Kliewer
A. B. Krisciunas
D. S. Kupperman (10)
M. Petrick
R. B. Poeppel (5)
A. C. Raptis
K. J. Reimann
J. J. Roberts
J. P. Singh
E. M. Stefanski
R. W. Weeks
C. A. Youngdahl
R. S. Zeno
ANL Patent Dept.
ANL Contract File
ANL Libraries (3)
TIS Files (6)

External:

DOE-TIC, for distribution per UC-25 (189)

DOE Chicago Operations Office:

Manager
D. L. Bray
F. Herbaty
V. H. Hummel

Materials Science and Technology Division Review Committee:

G. S. Ansell, Rensselaer Polytechnic Inst.
A. Arrott, Simon Fraser U.
A. L. Bement, TRW, Inc., Cleveland
R. C. Dynes, Bell Labs., Murray Hill
A. G. Evans, U. California, Berkeley
L. M. Falicov, U. California, Berkeley
H. K. Forsen, Bechtel Group, Inc., San Francisco
D. M. Ginsberg, U. Illinois, Urbana
E. Kay, IBM San Jose Research Lab.
M. E. Shank, Pratt & Whitney, East Hartford
P. G. Shewmon, Ohio State U.

U. S. Department of Energy, Washington:

Office of Fossil Energy:
J. P. Carr
S. J. Dapkunas
J. Fairbanks
C. L. Miller
M. I. Singer

Office of Energy Research:
J. S. Coleman
R. J. Gottschall
O. P. Manley
F. V. Nolfi
S. M. Wolf

Office of Vehicle and Engine Research and Development:
R. T. Alpaugh
A. A. Chesnes
C. Craig
D. P. Maxfield
R. P. Schulz
A. M. Zerega

Office of Coal Utilization Systems:
J. Birkeland

DOE Morgantown Energy Technology Center:

J. M. Hobday
A. J. Liberatore
J. Notestein
J. S. Wilson

DOE Idaho Operations Office:
W. H. Thielbahr
DOE Oak Ridge Operations Office:
E. E. Hoffman
DOE Pittsburgh Energy Technology Center:
J. D. Hickerson
Oak Ridge National Laboratory:
R. A. Bradley
R. Johnson
E. L. Long
R. W. McClung
A. C. Shaffhauser
V. J. Tennery
Other Government - University - Industry:
E. M. Anderson, Exxon Research and Engineering Co. Florham Park, N. J.
B. H. Baker, ARMCO, Inc., Middletown, O.
W. T. Bakker, Electric Power Research Inst., Palo Alto
G. Bandyopadhyay, GTE Labs., Inc., Waltham, Mass.
J. C. Benz, Cummins Engine Co., Columbus, Ind.
H. S. Berger, Industrial Quality, Inc., Gaithersburg, Md.
B. J. Berkowitz, Exxon Research and Engineering Co., Florham Park, N. J.
J. A. Bonar, Carborundum Co., Niagara Falls
R. C. Bradt, U. Washington
O. L. Buck, Ames Lab.
H. W. Carpenter, Rocketdyne Div., Rockwell International, Canoga Park
D. Cassidy, Ford Motor Co., Dearborn, Mich.
A. R. Ciuffreda, Exxon Research and Engineering Co., Florham Park, N. J.
M. Crowley, Amoco Research Center, Naperville, Ill.
W. M. Davis, Lava-Crucible Refractories Co., Zelienople, Pa.
C. J. Dobos, Gas Research Inst., Chicago
K. T. Faber, Ohio State U.
R. E. Farris, Kaiser Refractories, Pleasanton
N. F. Fiore, Cabot Corp., Boston
J. R. Friederichs, Combustion Engineering, Inc., Valley Forge, Pa.
E. Fuller, National Bureau of Standards, Washington
F. D. Gac, Los Alamos National Lab.
R. J. Gilmore, General Electric R&D Center, Schenectady
R. Greene, Johns Hopkins U.
B. Gustafson, Carborundum Co., Niagara Falls
S. D. Hartline, Norton Co., Worcester, Mass.
H. E. Helms, Allison Div., General Motors Corp., Indianapolis
R. H. Herron, Bethlehem Steel Corp. Homer Research Lab., Bethlehem, Pa.
V. Hill, Gas Research Inst., Chicago
R. Katz, Army Materials and Mechanics Research Center, Watertown, Mass.
C. R. Kennedy, Exxon Research and Engineering Co., Florham Park, N. J.
P. Khandelwal, Allison Div., General Motors Corp., Indianapolis
T. Khuri-Yakub, Stanford U.
G. Kino, Stanford U.
S. Klima, NASA Lewis Research Center
D. M. Kotchik, AiResearch Mfg. Co. of California, Torrance
V. Kotheri, Energy and Environmental Analysis, Inc., Arlington, Va.
E. H. Kraft, Kyocera International, Inc., San Diego
F. Lange, Rockwell International Science Center, Thousand Oaks, Calif.
E. Lenoe, Army Materials and Mechanics Research Center, Watertown, Mass.

J. R. Lewis, Rocketdyne Div., Rockwell International, Canoga Park
W. E. Leyda, Babcock & Wilcox Co., Alliance, O.
W. Loeffler, Siemens Medical Systems, Inc., Iselin, N. J.
W. Long, Babcock & Wilcox Co., Lynchburg
A. McLean, Ford Motor Co., Dearborn
J. Milewski, Los Alamos National Lab.
T. J. Miller, NASA Lewis Research Center
B. Probst, NASA Lewis Research Center
D. P. Reed, Norton Co., Worcester, Mass.
D. R. Richerson, AiResearch Mfg. Co., Phoenix
C. Robbins, National Bureau of Standards, Washington
D. W. Roy, Coors Porcelain Co., Golden, Colo.
R. W. Schleicher, General Atomic Co.
S. J. Schneider, National Bureau of Standards, Washington
J. Schuldies, AiResearch Mfg. Co., Phoenix
G. Sorell, Exxon Research and Engineering Co., Florham Park, N. J.
M. Srinivasan, Carborundum Co., Niagara Falls
G. Starr, Cummins Engine Co., Columbus, Ind.
J. Stringer, Electric Power Research Inst., Palo Alto
A. Vary, NASA Lewis Research Center
R. Viswanathan, Electric Power Research Inst., Palo Alto
M. E. Ward, Solar Turbines Intl., Div. Caterpillar Tractor Co., San Diego
G. W. Weber, Carborundum Co., Niagara Falls
S. Weiderhorn, National Bureau of Standards, Washington
D. R. Wilder, Iowa State U.
G. Willman, Dornier-System GmbH, Friedrichshafen, Germany
S. B. Young, Hague International, South Portland, Me.